Toward smaller aqueous-phase plasmonic gold nanoparticles: High-stability thiolate-protected ~ 4.5 nm cores

*M. Mozammel Hoque, Kathryn M. Mayer, Arturo Ponce, M. M. Alvarez, and Robert L. Whetten **

Department of Physics & Astronomy, University of Texas, San Antonio, Texas 78249, United States

ABSTRACT: Most applications of aqueous plasmonic gold nanoparticles benefit from control of the core size and shape, control of the nature of the ligand shell, and a simple and widely applicable preparation method. Surface functionalization of such nanoparticles is readily achievable but is restricted to water-soluble ligands. Here we have obtained highly monodisperse and stable *smaller* aqueous gold nanoparticles (core diameter ~ 4.5-nm), prepared from citrate-tannate precursors via ligand exchange with each of three distinct thiolates: 11-mercaptoundecanoic acid, α-R-lipoic acid, and para-mercaptobenzoic acid. These are characterized by UV-Vis spectroscopy for plasmonic properties; FTIR spectroscopy for ligand exchange confirmation; X-ray diffractometry for structural analysis; and high-resolution transmission electron microscopy for structure and size determination. Chemical reduction induces a blueshift, maximally +0.02-eV, in the LSPR band; this is interpreted as an electronic (-) charging of the MPC gold core, corresponding to a -0.5-V change in electrochemical potential.

INTRODUCTION

Monolayer protected clusters (MPCs) of noble metals can be considered as unique metallurgical molecules.[1-16] They have core-shell structures in which the metal core is encapsulated by a complete shell of covalently bonded ligands such as thiolates. This very thin monolayer of thiols generates an electrical double layer, known as the Stern layer, on the surface of gold nanoparticles, allowing gold nanoparticles to work as quantized double-layer (QDL) capacitors and store charge.[17-20] MPCs also possess the property of electric conduction when exposed to electromagnetic fields. These response processes, at once so alien to molecular chemistry yet so fundamental to metallurgy (including metallic colloids), are exemplified by the localized surface-plasmon resonances (LSPRs) in the optical spectra of gold-silver MPCs in dilute solutions.[1-16]

Gold nanoparticles in general have drawn a significant interest due to their inert nature to oxidation and corrosion and their unique optical and electronic properties.[21] Due to their localized surface plasmon resonance (LSPR) properties,[22] catalytic activity, and metallic nature, gold nanoparticles have been used in many applications including catalysis,[23-26] nanodevices,[27] sensor technology,[28-29] targeted drug delivery,[30-31] and other biomedical applications.[16, 32]

By exploiting their LSPR properties, smaller gold nanoparticles (< 6 nm diameter) can be efficiently applied for near-infrared photothermal cancer therapy treatment,[33] as at this specific size regime, nanoparticles can "effectively evade nonspecific uptakes by reticulo-endothelial system organs (e.g. liver, spleen)," and rather are rapidly cleared via the renal excretion mechanism (kidney).[34-35] Most of the potential applications of gold nanoparticles, especially in biomedical science, require highly stable water-soluble nanoparticles so that particles can tolerate an in vivo environment.[36] The citrate reduction method remains the most popular aqueous gold nanoparticle synthesis method, as first introduced by Turkevich *et al*.[37] and later modified by Frens *et al*.[38] An interesting feature is the flexible citrate layer on the surface of the nanoparticles which can be replaced with desired ligands.[39]

Noble-metal MPC molecules offer a number of advantages for the study of metallic response processes that are not available with more complex nanostructures. Atomic precision is exemplified by the recent crystallization of globular MPC molecules including Au_{279},[13] Au_{246},[40-41] and $(AgAu)_{267}$,[42] each ~ 2.1-nm core being protected by aromatic thiolate ligands. These substances may be stored indefinitely without deterioration. Their molecular masses are known, so that concentrations etc. can be determined with accuracy. From the atomic structure, theoretical methods to compute the various static and dynamic response properties may be tested. The substances may be concentrated, purified and generally handled like organic-terminated compact globular macromolecules, to which class of substances they evidently belong. No complicated apparatus is required for the high-yield preparation and purification of various species, in order to study the

growth and structure-dependent properties in a controlled, quantitative and chemically defined manner.

However, it is important here to note that each of the above mentioned products, of ~ 60 kDa mass (~ 2.1-nm core diameter) is *non-aqueous* (hydrophobic), as is the entire series recently developed by Kumara, Dass and coworkers: 75-kDa,[15] 120-kDa,[14] 207-kDa,[16] ~ 301-kDa,[1] and ~ 400-kDa[43] plasmonic hexanethiolate-protected nanocrystal gold molecules, of respective core-diameters ~ 2.2, 2.6, 3.1, 3.6, 4.0 nm.

In this present work, aqueous gold nanoparticles of core-diameter ~ 4.5 nm are initially synthesized by a modified Turkevich method.[32] Ligand-exchange reactions are then carried out with one of three thiolates 11-mercaptoundecanoic acid (MUA), α-R-Lipoic acid (LA), or para-mercaptobenzoic acid (pMBA),[6] resulting in thiolate-capped nanoparticles, henceforth referred to as Au-MUA, Au-LA, and Au-pMBA, respectively. All three ligands reported here a share the carboxylate terminal group (acidic, negative charge in solution), whereas base side/cationic[44-45] gold nanoclusters in the size range of 3.5 nm have been reported recently.[46] The resulting thiolate-protected, *water-soluble* ~ 4.5 nm gold nanoparticles have great development potential because they have masses, estimated at ~ 600-kDa (or 1.0 attogram), that lie just beyond the current upper limit of known MPC mass determinations,[1] or intermediate between the largest proteins and smallest viruses.

The product solutions are characterized by optical absorption (UV-Vis-NIR) spectroscopy to study their localized surface plasmon resonance (LSPR) band. The evidence of the complete exchange of citrate by the three distinct thiolate ligands is provided by optical vibrational spectroscopy (FTIR). Crystallite size and structure determination of the nanoparticle cores are inferred from independent measurements of X-ray diffraction (XRD), high resolution transmission electron microscopy (HR-TEM), and LSPR band of the UV-Vis spectra. Surface zeta potentials are also measured to study the colloidal stability. The localized surface plasmon resonance (LSPR) shift as a result of core charge on the gold nanoparticles due to increased electronic charge induced by different concentrations of sodium borohydride ($NaBH_4$) is also reported.

EXPERIMENTAL SECTION

Synthesis of Gold-Citrate-Tannate. The aqueous ~ 4.5 nm gold nanoparticle samples were prepared by an approach described elsewhere[47](as schematically presented in Figure S1). Briefly, 0.1 mL of 2.5 mM tannic acid [32, 48] was added into 150 mL of 2.2 mM trisodium citrate solution in ultrapure water under vigorous stirring. The pH of the solution was adjusted to ~ 11 using K_2CO_3. When the solution temperature reached 68-69 °C, 1 mL of 28 mM aqueous $HAuCl_4$ was added all at once. Instantly upon gold precursor injection, the solution color turned from transparent to dark gray, and then to a red wine color after 6-7 minutes.

Thiolate-exchange Reaction. The place-exchange reaction for MUA on as-synthesized citrate- capped gold nanoparticles was carried out following the same approach as followed for LA.[47]

Scheme 1. Molecular structure of ligands used in this work.

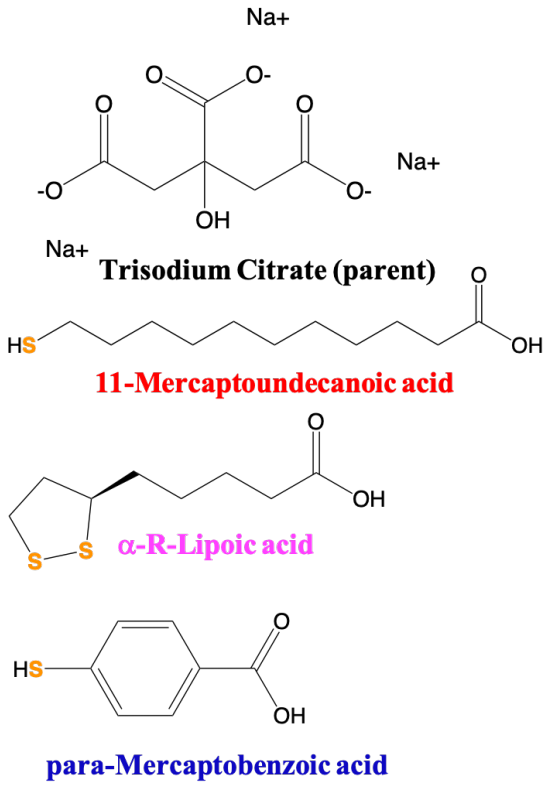

1.0 mM solution of MUA was prepared by adding NaOH to 5 mL pure H_2O until it dissolves completely. Then 100 µL of this MUA solution was added to 10 mL of as-synthesized gold nanoparticles and gently stirred overnight at room temperature for full complete exchange. pMBA ligand exchange was performed following the same procedure. To remove excess ligands and byproducts, nanoparticles were purified using a 10 kDa ultra-centrifuge filter (MWCO 10000, Amicon) by centrifugation at 10,000 rpm; first 10 mins for filtering, then 5 mins to collect the filtered samples. The optical absorbance spectra recorded before and after ligand exchange with three different thiols are presented in Figure 1.

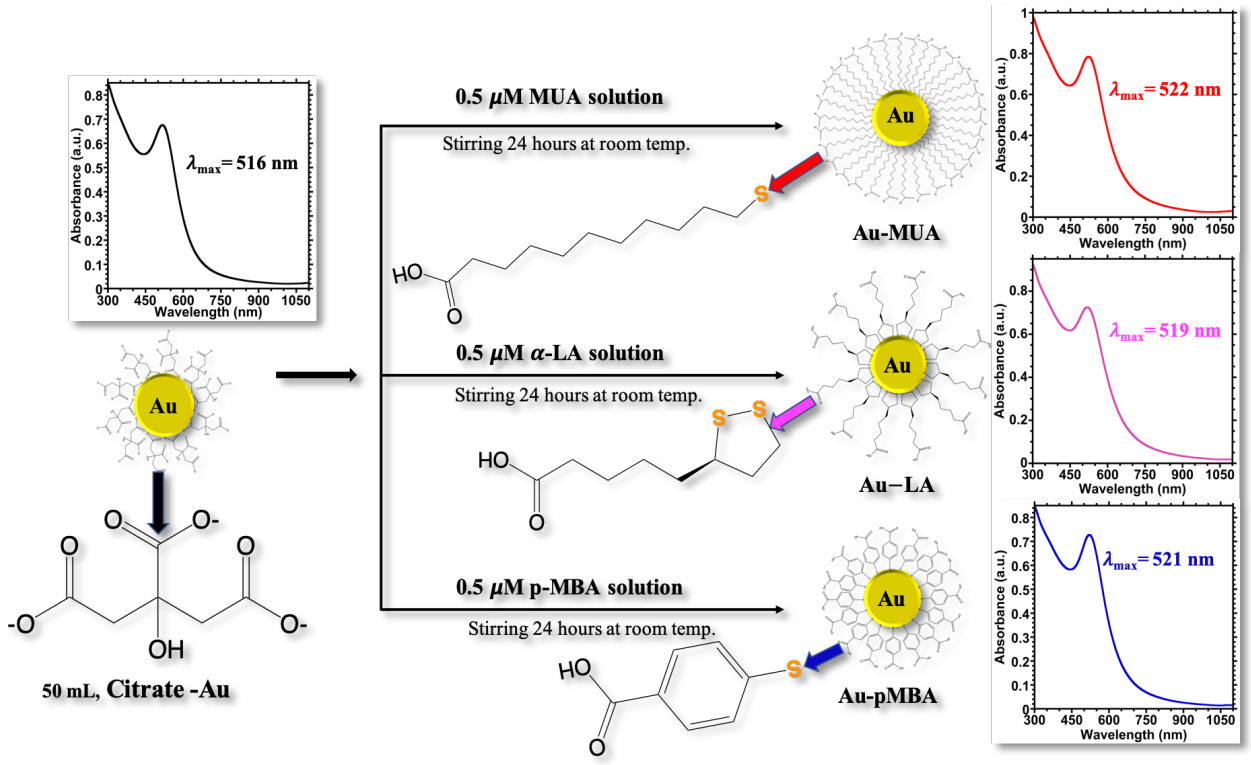

Figure 1. Thiol exchange reaction of as-synthesized aqueous ~ 4.5 nm gold nanoparticles with different thiols. Prior to ligand exchange the LSPR peak position is found at λ_{max} = 516 nm (left panel), but after ligand exchange LSPR red shifts of 6, 3, and 5 nm are observed for the cases of ligand exchange with MUA, LA, and pMBA respectively (right panel).

Sodium borohydride treatment on thiolated gold nanoparticles. To study the role of $NaBH_4$ in increasing electron density on the surface of gold nanoparticles capped with different thiols, a 100 mM sodium borohydride solution was freshly prepared then ice cooled before adding different amounts, i.e. 100 µL, 200 µL, and 300 µL to a separate cuvette containing 2 mL of Au-MUA solution. After adding the ice cooled $NaBH_4$ the mixture was rapidly mixed in a vortex before measurement of the LSPR by the UV-vis spectrometer. All instrumental methods and parameters for this work are described in the SI Section.

RESULTS AND DISCUSSION

A. Evidence of Ligand Exchange and Colloidal Stability. Evidence for the successful ligand exchange is the improvement in the practical stability of the particles with all three thiol ligands used (MUA, LA, and pMBA), as compared with the original citrate-gold colloid. Post-exchange, the material can be subjected to prolonged periods in boiling water (reflux), whereas the pre-exchange samples are most delicate. The material can also be dried and then redissolved quantitatively. The stability is further tested by freezing the samples; we have observed only thiolated gold can tolerate the freezing condition, whereas citrate capped Au NPs show irreversible aggregation. These are well established properties of MPCs due to the Au-S covalent bonding that are not possible for citrate- gold colloids.[1,13-16] UV-Vis spectra provide additional evidence of the ligand exchange.

The complete ligand exchange is further confirmed by Fourier transform infrared spectroscopy (FTIR) analysis as discussed below. All three types of thiol-exchanged nanoparticles studied, i.e., Au-MUA, Au-LA and Au-pMBA, exhibit high colloidal stability with high negative zeta potential at pH 8.0 as shown in Table S1. The physiochemical properties of the particles, i.e. surface zeta potential and electrophoretic mobility, showed high colloidal stability with high negative surface potential, though the zeta potential varies with the type of thiol used to protect the metal core of the particles.[49-50]

B. Optical Properties; UV-Vis Spectroscopy. Optical absorbance spectra (Figures 1-2) of dilute solution-phase samples, pre- or post-exchange, are always dominated by the broad LSPR band centered near 2.3-eV. Spectra are normalized at 4.0 eV for ease of comparison. Minimal or broadening in the lower energy (longer wavelength) range suggests negligible aggregation of the particles.[32] Figure

1B shows the effect of the purification process for Au-MUA (see Figure S5 for Au-LA and Au-pMBA), using an ultra-centrifuge filter, to remove the unbound ligands and other by-products of the reaction. Other

Figure 2A compares the absorbance spectrum of the initial citrate-protected gold nanoparticles with those of slightly smaller non-aqueous MPCs of known mass, 300 kDa (~ 3.6 nm)[1] and 400 kDa (~ 4.1 nm).[43] The aqueous citrate-protected gold nanoparticles show the LSPR peak maximum at the same energy of 2.34 eV or λ_m = 516 nm (see Figure S2A). This is consistent with the nanoparticles' mass and size range. The higher intensity of the LSPR peak of the 300 and 400 kDa MPCs could be due to the solvent refractive index, dielectric constant of the surrounding environment, thickness of the monolayer of ligand on the surface of the nanoparticles as thickness of the monolayer of ligand increases with the -CH_2 chain increment,[52-53] and the different types of ligands as compared to the 300 kDa and 400 kDa MPCs (hexanethiol protected).[1] Figures 2B and C compare the absorbance spectra of the various 4.5 nm aqueous thiolate-protected Au NPs. All three ligand capped Au NPs exhibited an LSPR red shift (Figure 1), though Au-MUA and Au-pMBA is the larger than Au-LA in comparison with citrate capped Au NPs (starting materials).

One may speculate as to how the ligand structure (or bonding) affects the LSPR bands of NPs protected by characterization methods (below) found no noticeable difference in terms of size, structure or morphology of the particles, indicating that the LSPR shift is due to the Au NPs' surface chemistry.[51]

three distinct thiols: It is observed that dithiols (lipoic acid) results in a smaller red shift of the LSPR peak, as compared with long chain monothiols (MUA) and aromatic thiols (pMBA). It is reported that dithiols make strong bonds with the metal core surface through two sulfur atoms.[54] pMBA is a monothiol, but unlike MUA possesses a proximal phenyl ring. These differences may affect the effective core size and local dielectric environment of the NPs, resulting in LSPR shifts.

The size of the particles may be estimated from UV-Vis spectra using Haiss' empirical formula,[55] according to which:

$$d(nm) = e^{(B_1 \frac{A_{LSPR}}{A_{450}} - B_2)} \qquad (1)$$

Here, A_{LSPR} is the absorbance at the LSPR peak, A_{450} is the absorbance at 450 nm, and B_1 = 3.00 and B_2 = 2.20 are empirical parameters (see Ref. 55 for details). From our spectra, citrate-capped Au NPs were calculated to have a diameter of 4.12±0.16 nm, versus 4.00±0.12 nm (MUA), 3.70±0.14 nm (LA), and 4.68±0.14 nm (pMBA). These contrast with direct measurements of the core diameter (below).

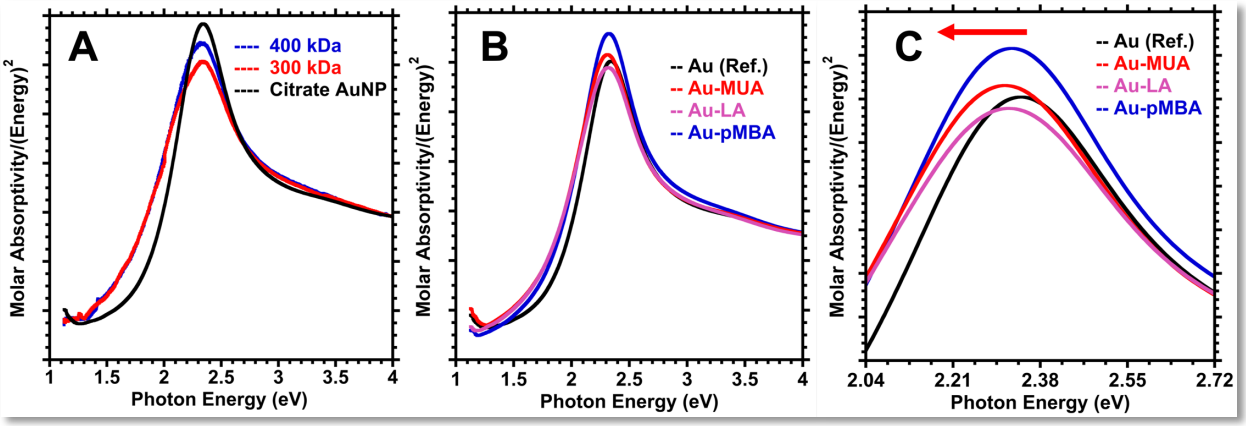

Figure 2. Optical absorption spectra of (A) Aqueous ~ 4.5 nm (citrate-capped) gold nanoparticles (black) in comparison with 300 kDa (red) and 400 kDa (blue) NPs. [1] (B) Original citrate acid-capped gold nanoparticles (black) in comparison with cleaned Au-LA (purple), Au-MUA (red), and Au-pMBA (blue). (C) Expanded version of B, showing red shift (arrow). Optical absorption spectrum of the nanoparticles is plotted against the photon energy, as the absorption divided by the energy (eV)^2, so that the relative peak areas in the energy spectrum preserve those in the original wavelength spectrum.[56]

C. Vibrational Properties; Fourier Transform Infrared Spectroscopy. FTIR analysis was performed to study the chemical adsorption of thiols on the surface of the NPs, or in other words, to confirm success of the ligand exchange procedures. Sample preparation and instrumental procedures are discussed in the supporting information section. For all ~ 4.5 nm gold NP samples, i.e., Au-MUA, Au-LA, and Au-pMBA, we have observed

a wide peak at 3400 cm^{-1} as shown in Figure 3. This peak is due to the O-H stretching of the molecules. The presence of the strong and sharp peaks at 2918 and 2848 cm^{-1} in the case of pure MUA thiol correspond to the asymmetric and symmetric stretching of CH_2 chains, respectively.[57-58]

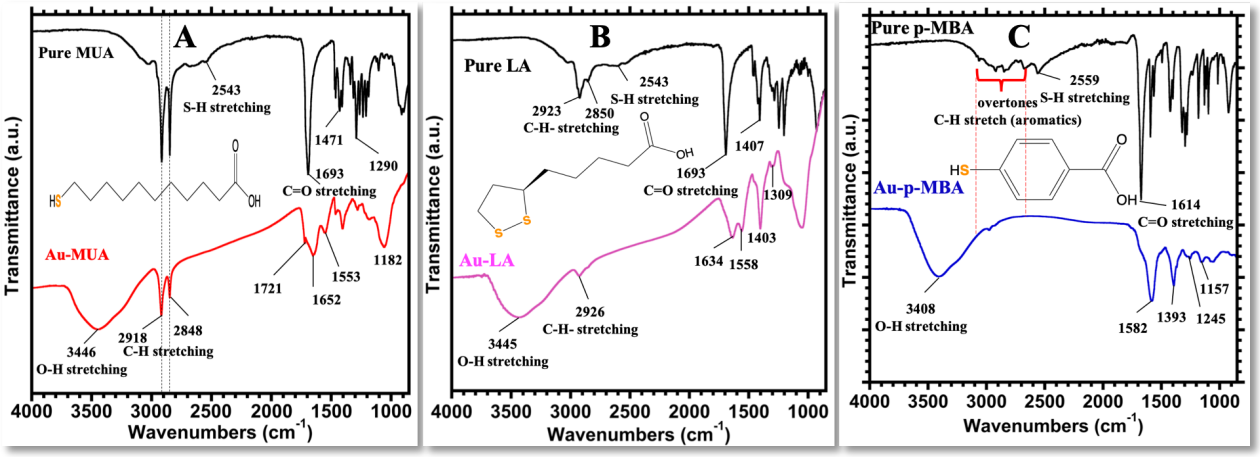

Figure 3. Evidence of the complete exchange of citrate by the various thiolate ligands is here provided by optical vibrational spectroscopy performed on powder samples of the respective samples. The transmittance FTIR spectra span the frequency range 4000-850 cm^{-1} of each neat thiol and the corresponding thiolate-protected gold NPs: (A) FTIR spectra of the neat MUA (black trace), a long methylene-chain thiol (inset shows the molecular structure of MUA) and the respective MUA-exchanged ~ 4.5-nm Au-MUA sample (red). (B) FTIR spectra of the neat dithiol lipoic acid (LA, in black; see molecular structure inset) and of the ~ 4.5-nm Au-LA (purple trace). C) FTIR spectra of the neat aromatic thiol pMBA (black trace, molecular structure inset) and of the ~ 4.5-nm Au-pMBA (blue). Each spectrum of respective gold-thiolate has been corrected by background subtraction of the KBr substrate.

These peaks are still present for ~ 4.5 nm Au-MUA after ligand exchange from citrate acid to MUA. In the case of pure LA, there are small and broad peaks at 2923 and 2850 cm^{-1}.[59-60] For ~ 4.5 nm Au-LA after ligand exchange from citrate acid to LA, the peak at 2850 cm^{-1} disappears and a very weak peak at 2926 cm^{-1} is observed. In the case of pure pMBA we have noticed overtones due to the C-H stretching of the aromatic ring that attached to the surface of the Au NPs after ligand exchange as shown in Figure 3C. [61-62] The appearance of a distinct peak at 1693 cm^{-1} for the case of pure MUA and LA, and at 1614 cm^{-1} for pure pMBA is due to the stretching of the carbonyl group (C=O) of the carboxylic acids. For all the spectra of pure thiols there is a small peak at ~ 2550 cm^{-1}, signifying S-H stretching. This peak disappears in the spectra of all three gold-thiols, which confirms that the thiols were attached to the surface of the Au NPs via Au-S bonds. This confirms the successful ligand exchange process. The peaks at ~1550 and ~1400 cm^{-1} for all three gold-thiol samples are due to the symmetric and asymmetric vibrations of the carboxylate groups present at the surface of the Au NPs. These outward-facing carboxyl groups can form strong hydrogen bonds with water molecules; this explains the long-lasting stability of these NPs in the aqueous phase.

D. X-ray Diffraction Analysis. X-ray powder diffraction (XRD) for metallurgical characterization is one of the most important non-destructive tools to analyze all kinds of matter—ranging from fluids, to powders and crystals. From research to production and engineering, XRD is an indispensable method for materials characterization and quality control. Prior to data analysis, X-ray detector position angle values (2θ) are converted into scattering vector (s) amplitudes:

$$s = 2sin\theta/\lambda \qquad (2)$$

Intensity, I(s), is then plotted versus scattering vector amplitude (s). The intensity data was background subtracted, and multiplied by s^2, to remove the strong peak asymmetry especially observed at low angle values. It is shown that the peak position (200) of aqueous ~ 4.5 nm nanoparticles with respect to scattering vector s is similar to that of 300 kDa NPs (Figure 4A), and peak position (111) peak is close to that of an ideal FCC

monocrystalline of truncated octahedral morphology, TO (5,5) Au_{1289}.[63]

To estimate an upper bound (neglecting effects of strain and twinning planes) on the crystallite size of nanoparticles from these powder X-ray diffraction patterns,[64] the Debye-Scherrer equation [65] is used. The XRD peak width is obtained for the (220) peak of the Au-LA XRD pattern, as this is the only peak that does not overlap with other peaks shown in Figure 4. According to the Debye-Scherrer formula, equation (2), the particle diameter, D, is given by:

$$D = k\lambda/\beta cos\theta = 0.94 * 0.154/\beta cos \quad (3)$$

where k is the Debye-Scherrer constant (k = 0.94 for spherical nanoparticles) and λ is the Cu $k\alpha$ radiation X-ray wavelength (λ = 0.154 nm). From Figure S5, we can see that the peak position 2θ = 65° and that the full width at half-maximum (FWHM), Δθ ≈ 4°. Converting Δθ from degrees to radians gives a peak broadening value of β = 0.07, yielding an estimated mean particle size of D = 4.7±0.1 nm. This value is slightly larger than the one calculated from optical absorption spectra for the citrate-capped NPs, Au-LA, and Au-MUA, but essentially the same as that calculated for the Au-pMBA.

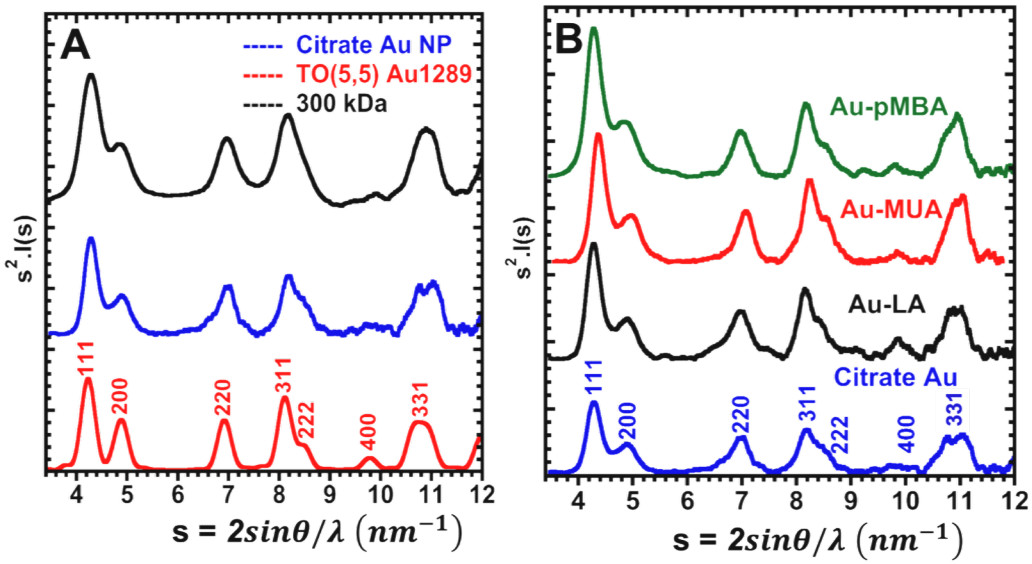

Figure 4. XRD patterns of (A) Citrate acid-protected AuNP (blue) compared with 300 kDa Au NPs (black) and ideal TO (5,5) Au_{1289} (red). (B) Citrate acid-protected AuNPs (blue) compared with ligand exchanged NPs with MUA (red), LA (black), and pMBA (light blue). Major peaks are shown at (111), (200), (220), (311), (222), (400), and (331).

E. High Resolution Transmission Electron Microscopy and Electron Diffraction Analysis. High-resolution transmission electron microscopy (HR-TEM) and electron diffraction methods provide a third approach to determine core size distributions and internal structure, provided that beam damage is minimized (low doses).

From the transmission electron microscopy (TEM) images in Figure 5, we can see that the nanoparticles are well dispersed with a uniform size distribution. A size distribution analysis for 4500 nanoparticles gave an estimate of 4.4 ± 0.5 nm, which closely agrees with the mean particle diameter obtained using the Debye-Scherrer formula and spans the range of values estimated from optical spectroscopy. The difference between TEM and XRD size calculations could be due to stress-induced peak broadening, which is not considered for the XRD analysis.

As-synthesized nanoparticles have FCC nanocrystalline structure of predominantly truncated octahedron (TOh) morphology with Wulff construction,[64-65] having thermodynamically stable surface atoms, but different morphologies from the cryogenic PDF fit analysis such as icosahedron or decahedron (dominantly) structures co-exist in the same sample.[47] The TEM study of Au-pMBA and Au-MUA did not show any significant difference in terms of size and disparity.

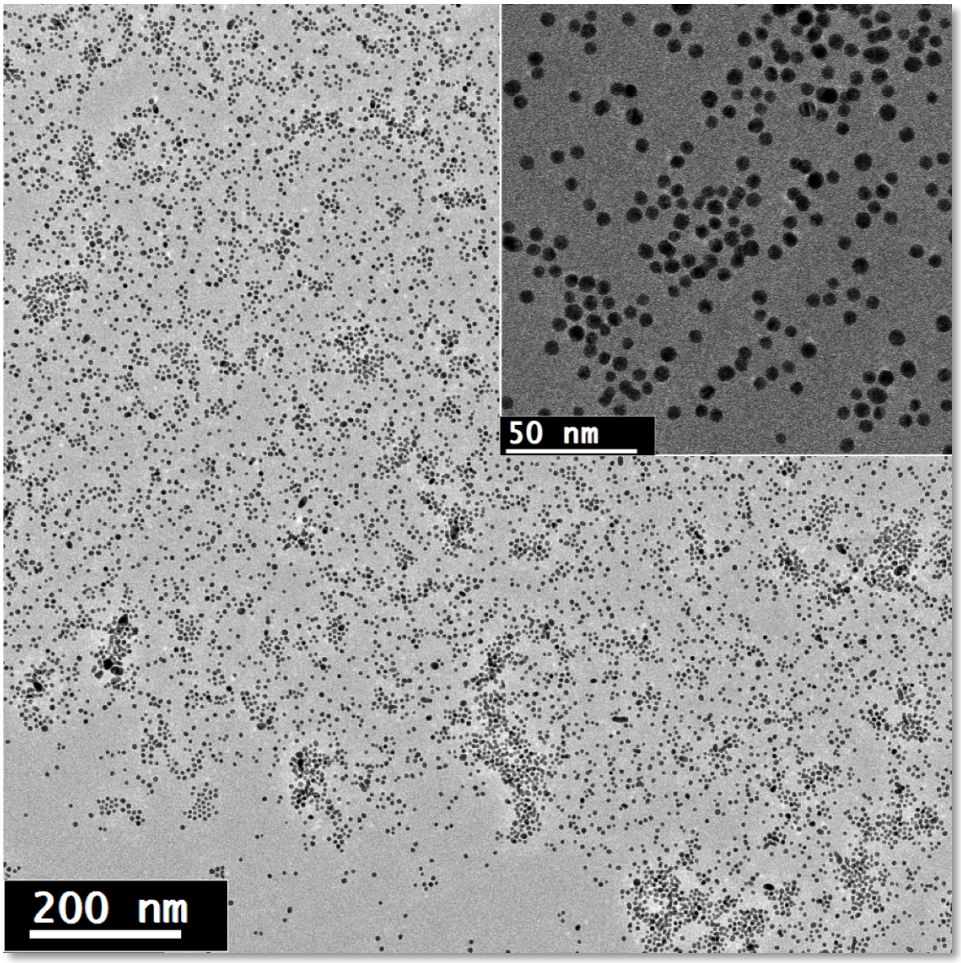

Figure 5. HR-TEM image of Au-LA NPs on holey carbon copper grid. Low magnification TEM image with high coverage showing particles are well dispersed. Inset: TEM micrograph with 50 nm scalebar showing spherical shape of the particles. See Figure S6 in the SI section for electron diffraction of ~ 4.5 nm gold nanoparticles.

F. Core Charging under Chemically Reducing Conditions. The sample preparation to investigate core charging of MPC core is explained in the supplementary information section. The LSPR position as a function of the number of free electrons in the metal core is given by, [53]

$$\frac{\lambda_{final}}{\lambda_{initial}} = \frac{eV_{initial}}{eV_{final}} = \left(\frac{N_{initial}}{N_{final}}\right)^{\frac{1}{2}} \qquad (4)$$

Here, we apply this equation to the case of Au-MUA core charging by sodium borohydride. According to the nano-scaling law[68] the aqueous ~ 4.5 nm gold nanoparticles have ~ 2800 gold atoms. If we assume one free electron per gold atom, then the initial number of electrons (N_{initial}) is 2800 and the LSPR position is 2.37 eV (eV_{initial}) as shown in Figure 7. (Note that all spectra are normalized to unity at $h\nu$ = 4.0 eV for ease of viewing.) Core charging by 100 μL and 200 μL of 100 mM sodium borohydride results in an LSPR blue shift to 2.38 eV (eV_{final}) by increasing the number of electrons on the metal core of the nanoparticles. Now, from Equation 4 we can find the increased number of free electrons to be ~ 24 (~ +1% increase). In the case where more sodium borohydride is added, i.e. 300 μ L of the same concentration in the same volume of MUA-protected gold nanoparticles, we can see a larger blue shift, with the number of additional free electrons being ~ 95 (+3%). If the volume or the concentration of the sodium borohydride increased more, i.e. either 300 mM or 500 μL of 100 mM then irreversible aggregation of the particles occurred.

According to Templeton *et al.*[46] electrolytic (+) charging of ~ 5.2-nm alkane-thiolate protected gold MPCs induced a *redshift* of +9 nm for a +0.98 V change in potential. Our chemical reduction induced a *blueshift* (maximally ~ +20 meV, or -4-5 nm), which by comparison to their results would indicate a maximal ~ -0.5 V reduction in electrochemical potential.

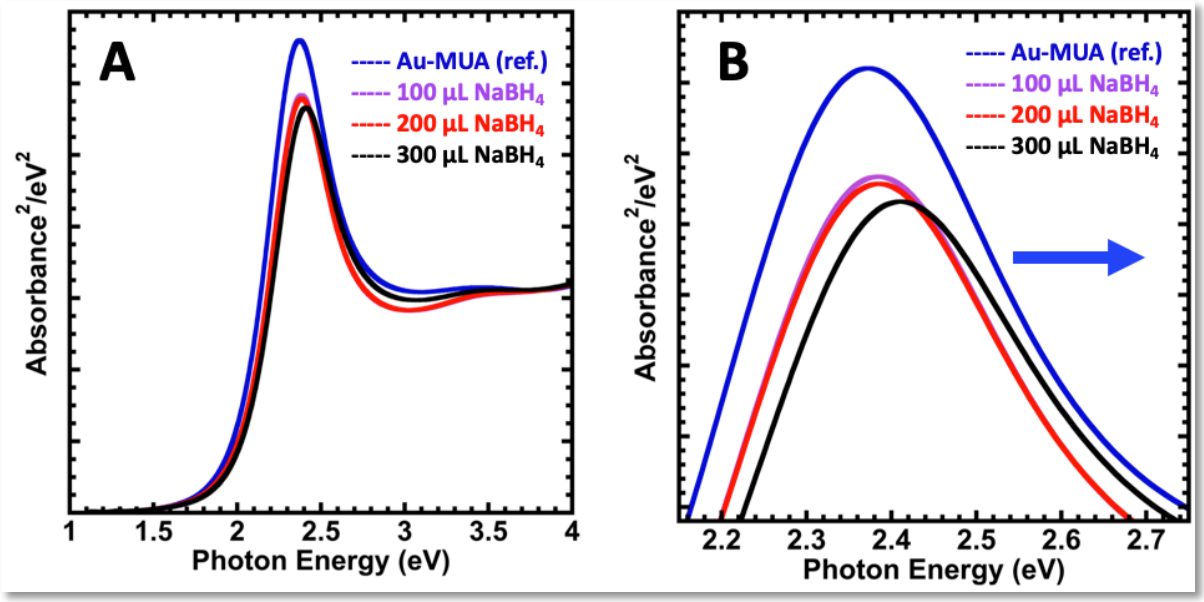

Figure 6. Second derivative optical absorption spectra of aqueous ~ 4.5 nm gold nanoparticles with core charging by the addition of different amounts of 100 mM sodium borohydride. (A) Core charging on MUA-protected Au NPs. (B) Expanded version of (A) to show details of the LSPR shift due to core charging. In all cases 2 mL of Au-MUA, has been used as a starting material. Second derivative ($\frac{abs^2}{eV^2}$) vs photon energy is plotted to elucidate plasmonic band position shift at lower energy,[53] arrow showing the direction of plasmonic shift.

CONCLUSION

In summary, aqueous plasmonic gold nanocrystals, of unprecedented small size, have been isolated in high yield and their key physico-chemical properties have been investigated. An efficient and robust solution-phase method to produce and purify these products is described and shown to give substances with molecule-like handling properties. Three (3) distinct thiolate ligands, all acid-terminated, are demonstrated:

α-LA, (lipoic acid, also known as thioctic acid, a 1,3-dithiolate natural product); MUA (a long-chain monothiolate, $-S(CH_2)_{10}COOH$); and pMBA (a conjugated aromatic thiolate, -SPhCOOH). Each is obtained by ligand exchange from precursor citrate-tannate gold sol. Independent estimates of the metallic core dimension gave the following values: From optical spectroscopy (LSPR band intensity and position): 4.24 nm (citrate-tannate precursor), vs. 4.00 nm (MUA), 3.76 nm (LA), and 4.74 nm (pMBA). From X-ray diffraction: Upper bound of ~ 4.8 nm (LA). From TEM: 4.4±0.5 nm (MUA). These dimensions (3.8 - 4.8 nm core diameter) relate well to recently obtained *non-aqueous* 300-kDa and 400-kDa hexanethiolate-protected gold nanocrystals (monolayer-protected clusters whose core diameters are ~ 3.6 and ~ 4.1 nm, respectively).

We have also observed that chemical reduction causes a significant blueshift in the localized surface plasmon resonance (maximally ~ +20 meV, or -4-5 nm), which by comparison to the effects of electrolytic (+) charging would indicate a ~ -500 mV reduction in electrochemical potential.

Exceptional contrast is obtained in high resolution TEM of single cores and precession electron diffraction (PED) over large numbers of cores, which yield a picture of globular nanocrystals with very high internal order, compatible with one or more modes of crystal growth and termination. A penta-twinned (decahedral) model gives an excellent fit to the pair-distribution function, extending to 2.0-nm interatomic distances. The high stability products are promising candidates for further

development, including bio-conjugation (involving the terminal carboxyl group); controlled etching and annealing to further refine the surface structure; and size separation of refined products to obtain aqueous-phase plasmonic gold nanocrystals with atomic or molecular precision. The efficiency and simplicity of the methods described herein should render them adaptable to a wider variety of metal and ligand combinations.

ASSOCIATED CONTENT

Supporting Information Available: Instrumental procedures and parameters for optical spectroscopy, optical vibrational spectroscopy (FTIR), X-ray diffraction, electron microscopy, and photon-correlation spectroscopy. Schematic representation of aqueous gold nanoparticles synthesis process, optical spectrum comparison for wavelength with photon energy, optical absorbance of thiol-functionalized gold nanoparticles before and after cleaning, zeta potential analysis table, sample preparation for the XRD and FTIR experiment, particle size determination from XRD pattern, electron micrograph and associated electron diffraction pattern.

This material is available free of charge via the internet at http://pubs.acs.org.

AUTHOR INFORMATION

CORRESPONDING AUTHOR

Whettenz60@gmail.com

NOTES

The authors declare no competing financial interests.

ACKNOWLEDGMENT

The authors thank Dr. M. J. Yacaman for access to use UV-Vis spectroscopy, Mr. Sean Mullins for helping with Au_{1289} structure-factor calculation, and Mr. James W. Boyd for helping with FTIR data collection. Microscopy was supported by the Kleberg Advanced Microscopy Center and the Nanotechnology and Human Health Core at UTSA, through the National Center for Research Resources (5G12RR013646-12). We also thank support from Department of Defense #72489-RT-REP and The Welch Foundation #AX-1857, "Fundamental Chemical Research on Larger Molecular Noble Metal Clusters".

REFERENCES

1. Kumara, C.; Hoque, M. M.; Zuo, X.; Cullen, D. A.; Whetten, R. L.; Dass, A., Isolation of a 300 kDa, $Au_{\sim 1400}$ Gold Compound, the Standard 3.6 nm Capstone to a Series of Plasmonic Nanocrystals Protected by Aliphatic-like Thiolates. *J. Phys. Chem. Lett.* **2018,** *9* (23), 6825-6832.
2. Schaaff, T. G.; Shafigullin, M. N.; Khoury, J. T.; Vezmar, I.; Whetten, R. L.; Cullen, W. G.; First, P. N.; Gutiérrez-Wing, C.; Ascensio, J.; Yacamán, M. J., Isolation of Smaller Nanocrystal Au Molecules: Robust Quantum Effects in Optical Spectra. *J. Phys. Chem. B* **1997,** *101* (40), 7885-7891.
3. Schaaff, T. G.; Knight, G.; Shafigullin, M. N.; Borkman, R. F.; Whetten, R. L., Isolation and Selected Properties of a 10.4 kDa Gold:Glutathione Cluster Compound. *J. Phys. Chem. B* **1998,** *102* (52), 10643-10646.
4. Schaaff, T. G.; Whetten, R. L., Giant Gold−Glutathione Cluster Compounds: Intense Optical Activity in Metal-Based Transitions. *J. Phys. Chem. B* **2000,** *104* (12), 2630-2641.
5. Alvarez, M. M.; Khoury, J. T.; Schaaff, T. G.; Shafigullin, M. N.; Vezmar, I.; Whetten, R. L., Optical Absorption Spectra of Nanocrystal Gold Molecules. *J. Phys. Chem. B* **1997,** *101* (19), 3706-3712.
6. Tvedte, L. M.; Ackerson, C. J., Size-Focusing Synthesis of Gold Nanoclusters with p-Mercaptobenzoic Acid. *J. Phys. Chem. A* **2014,** *118* (37), 8124-8128.
7. Knoppe, S.; Verbiest, T., Resonance Enhancement of Nonlinear Optical Scattering in Monolayer-Protected Gold Clusters. *J. Am. Chem. Soc.* **2017,** *139* (42), 14853-14856.
8. Bhattarai, N.; Black, D. M.; Boppidi, S.; Khanal, S.; Bahena, D.; Tlahuice, F. A.; Bach, S. B. H.; Whetten, R. L.; Yacaman, M. J., ESI-MS Identification of Abundant Copper–Gold Clusters Exhibiting High Plasmonic Character. *J. Phys. Chem. C* **2015,** *119* (20), 10935-10942.
9. Brust, M.; Kiely, C. J., Monolayer Protected Clusters of Gold and Silver. In *Colloids and Colloid Assemblies*, Wiley-VCH Verlag GmbH & Co. KGaA: 2004; pp 96-119.
10. Jin, R.; Zeng, C.; Zhou, M.; Chen, Y., Atomically Precise Colloidal Metal Nanoclusters and Nanoparticles: Fundamentals and Opportunities. *Chem. Rev.* **2016,** *116* (18), 10346-413.
11. Häkkinen, H.; Michael, W.; Grönbeck, H., Divide and Protect: Capping Gold Nanoclusters with Molecular Gold−Thiolate Rings. *J. Phys. Chem. B* **2006,** *110* (20), 9927-9931.
12. Jadzinsky, P. D.; Calero, G.; Ackerson, C. J.; Bushnell, D. A.; Kornberg, R. D., Structure of a thiol monolayer-protected gold nanoparticle at 1.1 Å resolution. *Science* **2007,** *318* (5849), 430-433.
13. Sakthivel, N. A.; Stener, M.; Sementa, L.; Fortunelli, A.; Ramakrishna, G.; Dass, A., $Au_{279}(SR)_{84}$: The Smallest Gold Thiolate Nanocrystal That Is Metallic and the Birth of Plasmon. *J. Phys. Chem. Lett.* **2018**, 1295-1300.
14. Kumara, C.; Zuo, X.; Ilavsky, J.; Chapman, K. W.; Cullen, D. A.; Dass, A., Super-stable, highly monodisperse plasmonic Faradaurate-500 nanocrystals with 500 gold atoms: $Au_{(\sim 500)}(SR)_{(\sim 120)}$. *J. Am. Chem. Soc.* **2014,** *136* (20), 7410-7.
15. Kumara, C.; Dass, A., $Au_{329}(SR)_{84}$ nanomolecules: compositional assignment of the 76.3 kDa plasmonic faradaurates. *Anal. Chem.* **2014,** *86* (9), 4227-32.
16. Kumara, C.; Zuo, X.; Cullen, D. A.; Dass, A., Faradaurate-940- Synthesis, Mass Spectrometry, Electron Microscopy, High-Energy X-ray Diffraction, and X-ray Scattering Study of $Au_{\sim 940 \pm 20}(SR)_{\sim 160 \pm 4}$ Nanocrystals. *Acs Nano* **2014,** *8* (6), 6431-6439.

17. Hicks, J. F.; Templeton, A. C.; Chen, S.; Sheran, K. M.; Jasti, R.; Murray, R. W.; Debord, J.; Schaaff, T. G.; Whetten, R. L., The Monolayer Thickness Dependence of Quantized Double-Layer Capacitances of Monolayer-Protected Gold Clusters. *Anal. Chem.* **1999,** *71* (17), 3703-3711.
18. Hicks, J. F.; Miles, D. T.; Murray, R. W., Quantized Double-Layer Charging of Highly Monodisperse Metal Nanoparticles. *J. Am. Chem. Soc.* **2002,** *124* (44), 13322-13328.
19. Chen, S.; Murray, R. W.; Feldberg, S. W., Quantized Capacitance Charging of Monolayer-Protected Au Clusters. *J. Phys. Chem. B* **1998,** *102* (49), 9898-9907.
20. Pietron, J. J.; Hicks, J. F.; Murray, R. W., Using Electrons Stored on Quantized Capacitors in Electron Transfer Reactions. *J. Am. Chem. Soc.* **1999,** *121* (23), 5565-5570.
21. Chakraborty, I.; Pradeep, T., Atomically Precise Clusters of Noble Metals: Emerging Link between Atoms and Nanoparticles. *Chem. Rev.* **2017,** *117* (12), 8208-8271.
22. Qian, H.; Zhu, Y.; Jin, R., Atomically precise gold nanocrystal molecules with surface plasmon resonance. *Proc. Natl. Acad. Sci.* **2012,** *109* (3), 696-700.
23. Sinha, A.; Seelan, S.; Tsubota, S.; Haruta, M., Catalysis by gold nanoparticles: epoxidation of propene. *Top. Catal.* **2004,** *29* (3-4), 95-102.
24. Grisel, R.; Weststrate, K.-J.; Gluhoi, A.; Nieuwenhuys, B. E., Catalysis by gold nanoparticles. *Gold Bull.* **2002,** *35* (2), 39-45.
25. Zhang, P.; Qiao, Z. A.; Jiang, X.; Veith, G. M.; Dai, S., Nanoporous ionic organic networks: stabilizing and supporting gold nanoparticles for catalysis. *Nano Lett.* **2015,** *15* (2), 823-828.
26. Oliver-Meseguer, J.; Doménech-Carbó, A.; Boronat, M.; Leyva-Pérez, A.; Corma, A., Partial reduction and selective transfer of hydrogen chloride on catalytic gold nanoparticles. *Angew. Chem.* **2017,** *129* (23), 6535-6539.
27. Haine, A. T.; Niidome, T., Gold Nanorods as Nanodevices for Bioimaging, Photothermal Therapeutics, and Drug Delivery. *Chem. Pharm. Bull.* **2017,** *65* (7), 625-628.
28. Kawawaki, T.; Zhang, H.; Nishi, H.; Mulvaney, P.; Tatsuma, T., Potential-Scanning Localized Plasmon Sensing with Single and Coupled Gold Nanorods. *J. Phys. Chem. Lett.* **2017,** *8* (15), 3637-3641.
29. Lin, X.; Ivanov, A. P.; Edel, J. B., Selective single molecule nanopore sensing of proteins using DNA aptamer-functionalised gold nanoparticles. *Chem. Sci.* **2017,** *8* (5), 3905-3912.
30. Pérez-Ortiz, M.; Zapata-Urzúa, C.; Acosta, G. A.; Álvarez-Lueje, A.; Albericio, F.; Kogan, M. J., Gold nanoparticles as an efficient drug delivery system for GLP-1 peptides. *Colloids Surf., B* **2017,** *158*, 25-32.
31. Du, Y.; Xia, L.; Jo, A.; Davis, R. M.; Bissel, P.; Ehrich, M. F.; Kingston, D. G., Synthesis and Evaluation of Doxorubicin-Loaded Gold Nanoparticles for Tumor-Targeted Drug Delivery. *Bioconjugate Chem.* **2018,** *29* (2), 420-430.
32. Piella, J.; Bastús, N. G.; Puntes, V., Size-Controlled Synthesis of Sub-10-nanometer Citrate-Stabilized Gold Nanoparticles and Related Optical Properties. *Chem. Mater.* **2016,** *28* (4), 1066-1075.
33. Hwang, S.; Nam, J.; Song, J.; Jung, S.; Hur, J.; Im, K.; Park, N.; Kim, S., A sub 6 nanometer plasmonic gold nanoparticle for pH-responsive near-infrared photothermal cancer therapy. *New J. Chem.* **2014,** *38* (3), 918-922.
34. Soo Choi, H.; Liu, W.; Misra, P.; Tanaka, E.; Zimmer, J. P.; Itty Ipe, B.; Bawendi, M. G.; Frangioni, J. V., Renal clearance of quantum dots. *Nat. Biotechnol.* **2007,** *25*, 1165.
35. Balogh, L.; Nigavekar, S. S.; Nair, B. M.; Lesniak, W.; Zhang, C.; Sung, L. Y.; Kariapper, M. S. T.; El-Jawahri, A.; Llanes, M.; Bolton, B.; Mamou, F.; Tan, W.; Hutson, A.; Minc, L.; Khan, M. K., Significant effect of size on the in vivo biodistribution of gold composite nanodevices in mouse tumor models. *Nanomed. Nanotechnol. Biol. Med.* **2007,** *3* (4), 281-296.
36. Rouhana, L. L.; Jaber, J. A.; Schlenoff, J. B., Aggregation-Resistant Water-Soluble Gold Nanoparticles. *Langmuir* **2007,** *23* (26), 12799-12801.
37. Turkevich, J.; Stevenson, P. C.; Hillier, J., A study of the nucleation and growth processes in the synthesis of colloidal gold. *Discuss. Faraday Soc.* **1951,** *11* (0), 55-75.
38. Frens, G., Controlled Nucleation for the Regulation of the Particle Size in Monodisperse Gold Suspensions. *Nat. Phys. Sci.* **1973,** *241*, 20.
39. Bastús, N. G.; Sánchez-Tilló, E.; Pujals, S.; Farrera, C.; López, C.; Giralt, E.; Celada, A.; Lloberas, J.; Puntes, V., Homogeneous Conjugation of Peptides onto Gold Nanoparticles Enhances Macrophage Response. *Acs Nano* **2009,** *3* (6), 1335-1344.
40. Zhou, M.; Zeng, C.; Song, Y.; Padelford, J. W.; Wang, G.; Sfeir, M. Y.; Higaki, T.; Jin, R., On the Non-Metallicity of 2.2 nm Au246 (SR) 80 Nanoclusters. *Angew. Chem.* **2017,** *129* (51), 16475-16479.
41. Higaki, T.; Zhou, M.; Lambright, K. J.; Kirschbaum, K.; Sfeir, M. Y.; Jin, R., Sharp transition from nonmetallic Au246 to metallic Au279 with nascent surface Plasmon resonance. *J. Am. Chem. Soc.* **2018,** *140* (17), 5691-5695.
42. Yan, J.; Malola, S.; Hu, C.; Peng, J.; Dittrich, B.; Teo, B. K.; Häkkinen, H.; Zheng, L.; Zheng, N., Co-crystallization of atomically precise metal nanoparticles driven by magic atomic and electronic shells. *Nat. Commun.* **2018,** *9* (1), 3357.
43. Vergara, S.; Santiago, U.; Kumara, C.; Alducin, D.; Whetten, R. L.; José Yacamán, M.; Dass, A.; Ponce, A. Synthesis, Mass Spectrometry and Atomic Structural Analysis of $Au_{\sim 2000}(SR)_{\sim 290}$ Nanoparticles. *J. Phys. Chem. C* **2018**, *122* (46), 26733–26738.
44. Hoque, M. M.; Black, D. M.; Mayer, K. M.; Dass, A.; Whetten, R. L., Base Side of Noble Metal Clusters: Efficient Route to Captamino-Gold, $Au_n(-S(CH_2)_2N(CH_3)_2)_p$, n = 25–144. *J. Phys. Chem. Lett.* **2019,** *10* (12), 3307-3311.
45. Ishida, Y.; Narita, K.; Yonezawa, T.; Whetten, R. L., Fully Cationized Gold Clusters: Synthesis of $Au_{25}(SR^+)_{18}$. *J. Phys. Chem. Lett.* **2016,** *7* (19), 3718-3722.
46. Hoque, M. M.; Dass, A.; Mayer, K. M.; Whetten, R. L., Protein-Like Large Gold Clusters Based on the ω-Aminothiolate DMAET: Precision Thermal and Reaction Control Leading to Selective Formation of Cationic Gold Clusters in the Critical Size Range, n = 130–144 Gold Atoms. *J. Phys. Chem. C* **2019,** *123* (23), 14871-14879.

47. Hoque, M. M.; Vergara, S.; Dass, P. P.; Ugarte, D.; Santiago, U.; Kumara, C.; Whetten , R. L.; Dass , A.; Ponce, A., Structural Analysis of Ligand Protected Smaller Metallic Nanocrystals by Atomic Pair Distribution Function Under Precession Electron Diffraction. *J. Phys. Chem. C* **Under revision**
48. Giersig, M.; Mulvaney, P., Preparation of ordered colloid monolayers by electrophoretic deposition. *Langmuir* **1993,** *9* (12), 3408-3413.
49. Bastús, N. G.; Piella, J.; Puntes, V., Quantifying the sensitivity of multipolar (dipolar, quadrupolar, and octapolar) surface plasmon resonances in silver nanoparticles: the effect of size, composition, and surface coating. *Langmuir* **2015,** *32* (1), 290-300.
50. Pensa, E.; Cortés, E.; Corthey, G.; Carro, P.; Vericat, C.; Fonticelli, M. H.; Benitez, G.; Rubert, A. A.; Salvarezza, R. C., The chemistry of the sulfur–gold interface: in search of a unified model. *Acc. Chem. Res.* **2012,** *45* (8), 1183-1192.
51. Templeton, A. C.; Pietron, J. J.; Murray, R. W.; Mulvaney, P., Solvent Refractive Index and Core Charge Influences on the Surface Plasmon Absorbance of Alkanethiolate Monolayer-Protected Gold Clusters. *J. Phys. Chem. B* **2000,** *104* (3), 564-570.
52. Mooney, J.; Kambhampati, P., Correction to "Get the Basics Right: Jacobian Conversion of Wavelength and Energy Scales for Quantitative Analysis of Emission Spectra". *J.Phys. Chem. Lett.* **2014,** *5* (20), 3497-3497.
53. Abad, J. M.; Mertens, S. F.; Pita, M.; Fernández, V. M.; Schiffrin, D. J., Functionalization of thioctic acid-capped gold nanoparticles for specific immobilization of histidine-tagged proteins. *J. Am. Chem. Soc.* **2005,** *127* (15), 5689-5694.
54. Haiss, W.; Thanh, N. T.; Aveyard, J.; Fernig, D. G., Determination of size and concentration of gold nanoparticles from UV− Vis spectra. *Anal. Chem.* **2007,** *79* (11), 4215-4221.
55. Amoli, B. M.; Gumfekar, S.; Hu, A.; Zhou, Y. N.; Zhao, B., Thiocarboxylate functionalization of silver nanoparticles: effect of chain length on the electrical conductivity of nanoparticles and their polymer composites. *J. Mater. Chem.* **2012,** *22* (37), 20048-20056.
56. Jeshari, H. H.; Nejad, H. R.; Kahkhaie, V. R.; Deymehkar, E., Applying the synthesized gold nanoparticles and investigating the effect of ligand-functionalized nanoparticles on efficiency of dye sensitized solar cells. *Adv. Nat. Sci.* **2018,** *9* (3), 035017.
57. Wang, J.; Xia, Q., Alpha-lipoic acid-loaded nanostructured lipid carrier: sustained release and biocompatibility to HaCaT cells in vitro. *Drug Delivery* **2014,** *21* (5), 328-341.
58. Zhang, H.; Liu, M.; Huang, G.; Yu, Y.; Shen, W.; Cui, H., Highly chemiluminescent gold nanopopcorns functionalized by N-(aminobutyl)-N-(ethylisoluminol) with lipoic acid as a co-stabilizing reagent. *J. Mater. Chem. B* **2013,** *1* (7), 970-977.
59. Zhou, Y.; Zhao, H.; Li, C.; He, P.; Peng, W.; Yuan, L.; Zeng, L.; He, Y., Colorimetric detection of Mn^{2+} using silver nanoparticles cofunctionalized with 4-mercaptobenzoic acid and melamine as a probe. *Talanta* **2012,** *97*, 331-335.
60. Zhou, Y.; Zhao, H.; He, Y.; Ding, N.; Cao, Q., Colorimetric detection of Cu^{2+} using 4-mercaptobenzoic acid modified silver nanoparticles. *Colloids Surf., A* **2011,** *391* (1-3), 179-183.
61. Luedtke, W.; Landman, U., Structure and thermodynamics of self-assembled monolayers on gold nanocrystallites. *J. Phys. Chem. B* **1998,** *102* (34), 6566-6572.
62. Burton, A. W.; Ong, K.; Rea, T.; Chan, I. Y., On the estimation of average crystallite size of zeolites from the Scherrer equation: A critical evaluation of its application to zeolites with one-dimensional pore systems. *Microporous Mesoporous Mater.* **2009,** *117* (1), 75-90.
63. Scherrer, P., Determination of the size and internal structure of colloidal particles using X-rays. *Nachr. Ges. Wiss. Göttingen* **1918,** *2*, 98-100.
64. Morgan, F.; French, C.; Greenleaf, S., Wulff clusters in R^2. *J. Geom. Anal.* **1998,** *8* (1), 97.
65. Ringe, E.; Van Duyne, R. P.; Marks, L. D., Wulff construction for alloy nanoparticles. *Nano. Lett.* **2011,** *11* (8), 3399-403.
66. Dass, A., Nano-scaling law: geometric foundation of thiolated gold nanomolecules. *Nanoscale* **2012,** *4* (7), 2260-2263.
67. Plascencia-Villa, G.; Demeler, B.; Whetten, R. L.; Griffith, W. P.; Alvarez, M.; Black, D. M.; José-Yacamán, M., Analytical Characterization of Size-Dependent Properties of Larger Aqueous Gold Nanoclusters. *J. Phys. Chem. C* **2016,** *120* (16), 8950-8958.
68. Wang, W.; Ding, X.; Xu, Q.; Wang, J.; Wang, L.; Lou, X., Zeta-potential data reliability of gold nanoparticle biomolecular conjugates and its application in sensitive quantification of surface absorbed protein. *Colloids Surf., B* **2016,** *148*, 541-548.

TOC Graphic

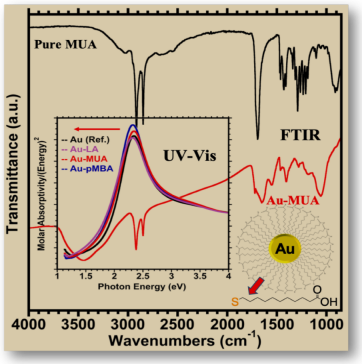
Pure MUA
FTIR
UV-Vis
Au (Ref.)
Au-LA
Au-MUA
Au-pMBA
Molar Absorptivity/(Energy)²
Photon Energy (eV)
Au-MUA
Au
S
OH
Transmittance (a.u.)
Wavenumbers (cm⁻¹)